RSC Advances

PAPER

Cite this: *RSC Adv.*, 2017, 7, 32133

Ferromagnetic-like behaviour in bismuth ferrite films prepared by electrodeposition and subsequent heat treatment†

Doga Bilican,[a] Enric Menéndez,*[a] Jin Zhang,[a] Pau Solsona,[a] Jordina Fornell,[a] Eva Pellicer *[a] and Jordi Sort[ab]

Bismuth ferrite ($BiFeO_3$) films (10 μm in thickness) are synthesized by electrodeposition from a dimethylformamide bath containing Bi and Fe nitrate salts as precursors followed by heat treatment in air. Thermal treatments are needed to induce crystallisation of the as-deposited amorphous-like films. A detailed morphological, structural and magnetic characterisation evidences that $BiFeO_3$ forms in a rather narrow temperature window (around 600 °C). At lower and higher temperatures, secondary binary and ternary oxides are also formed. Soft ferromagnetic-like behaviour is observed in all films, which presumably arises from the obtained nanoscale structure, which favours the occurrence of spin canting in the $BiFeO_3$ antiferromagnetic phase. The eventual contribution from secondary phases to the observed ferromagnetic-like response is also discussed. The obtained results are appealing for the integration of $BiFeO_3$ into devices that may require relatively thick films with an enhanced surface area-to-volume ratio. The growth of this type of material by techniques other than electrodeposition is not straightforward.

Received 18th April 2017
Accepted 16th June 2017

DOI: 10.1039/c7ra04375a

rsc.li/rsc-advances

Introduction

The primary physical mechanisms of ferroelectricity and magnetism are different and tend to exclude each other.[1] However, both phenomena may coexist in the so-called multiferroic materials.[1,2] These materials show coupled ferroelectric and magnetic properties. That is, magnetism can be controlled through electric fields and *vice versa*. From a technological viewpoint, this provides increased degrees of freedom in the design and energy-efficient manipulation of spintronic and memory devices.[1,2] Since these devices are ultimately controlled by electric currents, their operation involves considerable energy loss by the Joule heating effect. Thus, the partial substitution of electric currents by electric fields (*i.e.*, voltage-driven magnetic actuation) would significantly decrease the overall power consumption.[3,4]

Among the few materials which exhibit intrinsic multiferroicity, $BiFeO_3$ (BFO) is attracting huge interest since it is both ferroelectric and antiferromagnetic at room temperature (its ferroelectric Curie temperature is 770 °C, while its Néel temperature is around 370 °C (ref. 1, 2 and 5)). BFO crystallises in a rhombohedral ($R3c$) structure and belongs to the group of perovskites with the ABO_3 formula.[2] From a thermodynamic point of view, $BiFeO_3$ is a metastable compound that exists between the stable $Bi_{25}FeO_{39}$ (sillenite) and $Bi_2Fe_4O_9$ (mullite) compounds according to the equilibrium phase diagram of Bi_2O_3 and Fe_2O_3.[2,6] It actually forms between 447 °C and 767 °C. Nevertheless, BFO has a high tendency to grow simultaneously with these other two stable phases. The quality of the end product depends on several factors, such as purity of the precursors, preparation method, chemical additives or heat treatment conditions.[7–10] The properties of BFO are indeed very sensitive to oxygen stoichiometry and tiny deviations might lead to undesired properties, such as strong current leakages.[11] Furthermore, although BFO is antiferromagnetic, it often shows soft ferromagnetism which originates from spin canting.[2,12] Interestingly, larger saturation magnetisation is achieved due to size-effects (in samples with reduced lateral dimensions) since spin canting reinforces due to the partial suppression of the spiral spin structure.[13] In this context, the development of nanoscale architectures becomes crucial to engineer novel magnetoelectric materials.[14,15] Remarkably, besides its potential applications in spintronics and data storage, BFO is a suitable candidate to be used also in photovoltaic devices and related applications.[16–18]

A wide variety of growth techniques and post-synthesis treatments have been used to prepare BFO. Solid state reaction,[9] sol–gel,[19,20] pulsed laser deposition,[21,22] sputtering,[23] solution combustion,[24] aqueous gel precursors,[25] microemulsion,[26] the

---

[a] *Departament de Física, Facultat de Ciències, Universitat Autònoma de Barcelona, E-08193 Bellaterra, Spain. E-mail: enric.menendez@uab.cat; eva.pellicer@uab.cat*

[b] *Institució Catalana de Recerca i Estudis Avançats (ICREA), Pg. Lluís Companys 23, 08010 Barcelona, Spain*

† Electronic supplementary information (ESI) available: Further details on the Rietveld refinements. See DOI: 10.1039/c7ra04375a

Pechini method[27] or microwave hydrothermal synthesis[28] are amongst the most frequently employed. A fast-growing research has been devoted to the manufacture and characterisation of BFO nanoscopic shapes, such as nanofibers,[29] nanowires,[30] nanotubes,[29,31] or nanoparticles.[32] These nanostructures offer distinctive size effects which, as previously explained, can affect some of the physical properties of BFO.

Some of the aforementioned techniques (solid state reaction, sol–gel or solution combustion) typically render powdery BFO, thus hindering its eventual integration into devices since it would need further immobilization on a substrate. Usually, smooth coatings with compositional homogeneity are successfully obtained by pulsed laser deposition. However, this method is a costly method since it requires high vacuum conditions. Moreover, it does not allow the growth of micrometre-thick films, neither the deposition onto curved substrates nor the control of film's porosity.

Interestingly, electrodeposition enables the low-cost growth of relatively thick films directly on a substrate with a simple setup. Besides its obvious use for the growth of pure metals and metallic alloys, electrodeposition is a powerful methodology that can be utilized for the preparation of semiconducting metal oxides, hydroxides and chalcogenides, either in the form of films or nanostructures.[33–36] So far, investigation on BFO electrodeposition has been very scarce and the results have not been fully satisfactory in the sense that they lack a clear and unambiguous structural characterisation.[37–39] Moreover, in these previous works, emphasis was laid on the electrochemical performance of the materials (*i.e.*, BFO nanoflake and thin films electrodes were applied in supercapacitor applications). The magnetic properties were overlooked.

To the best of our knowledge, here we report for the first time the formation of rhombohedral BFO phase by cathodic electrodeposition from a novel *N*,*N*-dimethylformamide (DMF) bath and subsequent thermal treatment. Fe(III) and Bi(III) nitrate salts have been solubilized in the organic electrolyte. Interestingly, the applied electrodeposition conditions render rough, not fully dense (porous-like), BFO films. Heat treatments at various annealing temperatures are performed in order to investigate the crystallisation behaviour of the as-prepared BFO. These materials are further studied from a magnetic point of view. Ferromagnetic-like properties stemming from finite size effects (spin canting) are observed.

Experimental

10 μm-thick, amorphous-like films with Bi : Fe ≈ 1 were deposited on Si/Ti/Cu substrates by potentiostatic electrodeposition from a bath containing 6 g L^{-1} $Bi(NO_3)_3 \cdot 5H_2O$ (Sigma-Aldrich, ≥98.0%) and 10 g L^{-1} $Fe(NO_3)_3 \cdot 9H_2O$ (Sigma-Aldrich, ≥99.95%) dissolved in DMF (Sigma-Aldrich, ≥99.8%). A three-electrode cell with a Pt wire as counter electrode and a Ag|AgCl (3 M KCl) reference electrode ($E = +0.210$ V NHE) was used. The configuration (*i.e.*, arrangement and separation) of the electrodes was kept the same in all experiments (cyclic voltammetry (CV) and electrodeposition). Specifically, depositions were carried out under direct current conditions at 28 °C for 1800 s, while stirring the bath at 200 rpm. Unless otherwise stated, the cathodic potential applied was −1.3 V. The working area was kept between 0.250 and 0.275 cm^2. After electrodeposition, the samples were rinsed in Milli-Q water and hot dried. Coating thickness was measured with a 3D Optical Surface Metrology System Leica DCM 3D. Subsequently, with the aim to investigate the crystallisation behaviour and ultimately to obtain crystalline $BiFeO_3$, the as-deposited samples were subjected to different thermal treatments in a Carbolite MTF 9/15/130 tubular furnace in open atmosphere at 500, 600, 700 and 800 °C for 2 hours. The samples were heated at a rate of 1 °C min^{-1} and cooled down in air. A Merlin ZEISS scanning electron microscope was used to investigate the morphology of the samples using secondary electrons. The structural characterisation was done by means of $\theta/2\theta$ X-ray diffraction (XRD) using Cu K_α radiation. Furthermore, Rietveld refinements of the XRD patterns using the MAUD software[40,41] were carried out to determine the crystallite size (*i.e.*, average coherently diffracting domain size) of the main phases (further details on the Rietveld refinements can be found in the ESI†). Transmission electron microscopy (TEM) analyses were done on a Jeol JEM-2011 microscope operated at 200 kV. Finally, the samples were magnetically characterised by recording the magnetisation (M) *vs.* applied magnetic field (H_{applied}) curves (*i.e.*, hysteresis loops) by means of vibrating sample magnetometry (Microsense from LOT-QuantumDesign) at room temperature.

Results and discussion

Electrochemical deposition

Metals and metal matrix/nanoparticle composites have been deposited from DMF in the past.[42,43] The examples available, although scarce compared to water-based electrolytes, mainly focus on cobalt, nickel and their alloys. Little is known about the electrodeposition of metal oxides from DMF baths. In our laboratory, attempts to produce Bi- and Fe-containing films with Bi : Fe ≈ 1 from aqueous solution (0.045 M $Fe(NO_3)_3 \cdot 9H_2O$, 0.01 M $Bi(NO_3)_3 \cdot 5H_2O$ and 0.1 M triethanolamine) failed. In particular, only Bi-rich deposits were obtained at pH 12.5 and $T = 65$ °C for deposition potentials ranging from −0.8 V to −1.5 V. On the contrary, codeposition of both Bi and Fe elements in comparable amounts was possible from the DMF bath. This is because the deposition potentials in water and DMF media are different.

Fig. 1a shows the CV curve recorded from the DMF bath under stagnant conditions. Negative currents were detected from +0.25 V during the cathodic going sweep. Prior to reversing the scan toward anodic potentials, a diffusion-controlled peak was recorded at −1.1 V. Fig. 1b shows the *j*–*t* curves recorded between −1.25 V and −1.35 V under stagnant conditions. Whilst less negative currents were observed for an applied potential of −1.25 V during the first 200 s of deposition, fluctuations caused the currents to almost merge afterwards. A similar trend was observed under stirred conditions (see inset of Fig. 1b). In this case the *j*–*t* transients showed even more pronounced fluctuations. Since the currents were similar, −1.30 V was selected for the subsequent growth of BFO films.

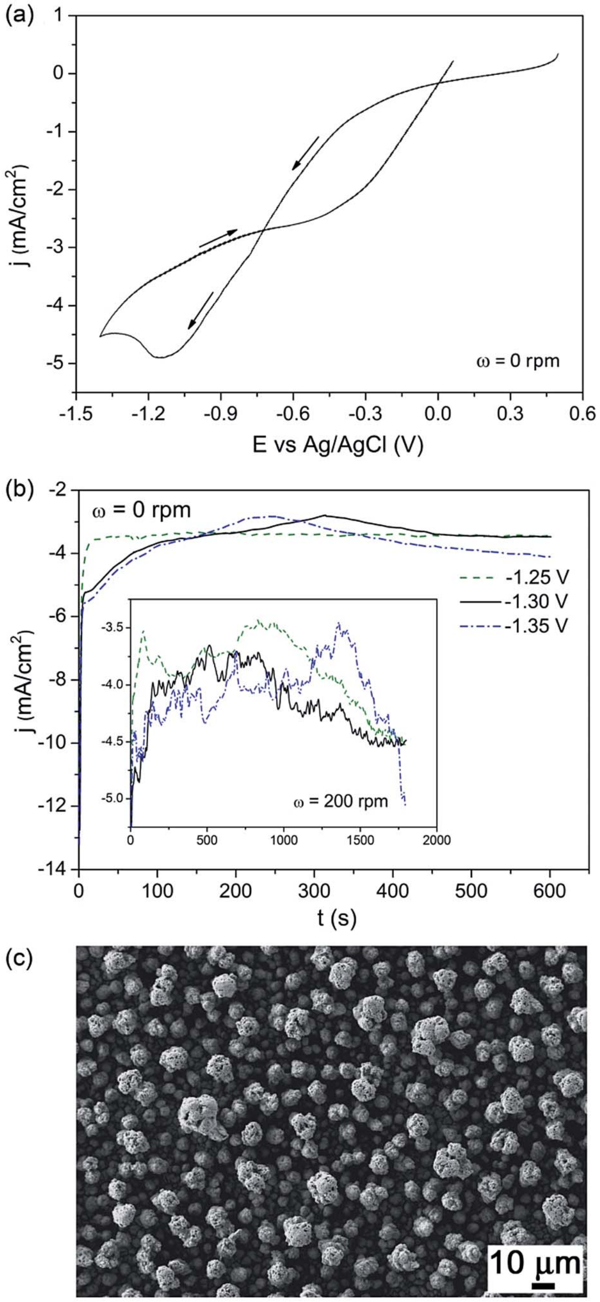

Fig. 1 (a) CV curve recorded under quiescent conditions, initially scanning from +0.5 V toward negative potentials, at 50 mV s^{-1}. (b) j–t curves recorded under stagnant conditions at −1.25 V, −1.30 V and −1.35 V for 600 s. The inset shows the j–t curves recorded at the same potentials but under stirred conditions ($\omega = 200$ rpm) for longer deposition time (1800 s). (c) SEM image, taken with secondary electrons, of an as-electrodeposited film at −1.30 V for 1800 s.

Fig. 1c shows a scanning electron microscopy (SEM) image of an as-deposited film. A rough morphology consisting of not fully dense nodules was noticed. At a low magnification, the coating displayed a cracked appearance, likely caused by layer dehydration in the SEM vacuum chamber. The presence of small amount of water is unavoidable when using DMF as solvent. These cracks are frequently observed in metal oxides produced by electrodeposition in aqueous solutions.[34]

Structural and morphological characterisation

The XRD pattern of the as-deposited sample (not shown) is consistent with an amorphous-like phase since, besides peaks arising from the substrate, only wide halos are observable. As can be seen in Fig. 2, crystallisation takes place upon heat treatment. At 500 °C, rhombohedral BFO with a crystallite of around 42 nm is formed together with Bi_2O_3, Fe_2O_3, Fe_3O_4 and ternary oxides, such as $Bi_{24}Fe_2O_{39}$ or $Bi_2Fe_4O_9$. According to the phase diagram,[2] the presence of these phases indicates that 500 °C is still a mild condition for the BFO formation.

From a thermodynamic point of view, BFO is formed from equal parts of Bi_2O_3 and Fe_2O_3. Upon annealing at 600 °C, the amount of BFO further increases in detriment mainly of Bi_2O_3 and Fe_2O_3, becoming nearly the only phase. The crystallite size grows up to around 80 nm, suggesting that ternary phases, which tend to grow at the grain boundaries of BFO, have strongly vanished, as suggested by the XRD characterisation. The thermal treatment at 700 °C leads to a significant formation of $Bi_2Fe_4O_9$ at expenses of $BiFeO_3$, which still shows an increased crystallite size (about 146 nm). In turn, the crystallite size of the $Bi_2Fe_4O_9$ phase is around 100 nm. The relatively large crystallite size of BFO suggests that $Bi_2Fe_4O_9$ grows in cluster-like form rather than precipitate-like at the grain boundaries of BFO, which would result in a decreased BFO crystallite size. Upon annealing at 800 °C, $Bi_2Fe_4O_9$ becomes the main phase. In comparison with BFO, this ternary phase is an Fe-rich phase, thus, to keep the stoichiometry, Fe-free phases must be formed. As expected, the XRD pattern of the sample thermally treated at 800 °C shows that $Bi_2Fe_4O_9$ forms along with Bi_2O_3 and

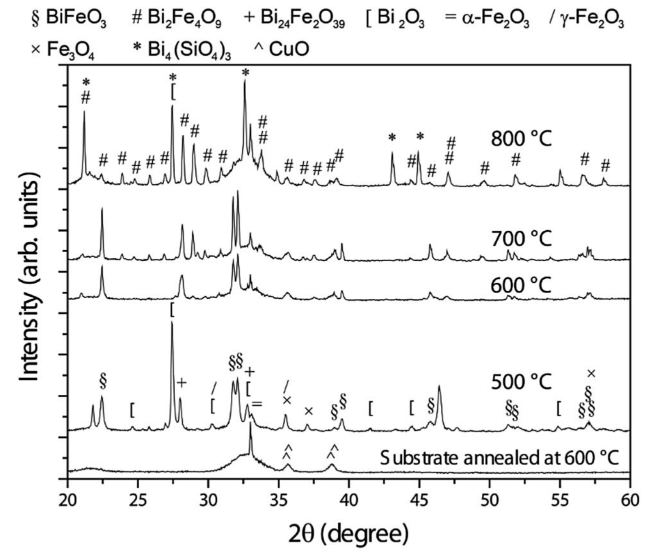

Fig. 2 $\theta/2\theta$ X-ray diffraction patterns of the samples annealed at 500, 600, 700 and 800 °C. To serve as reference, the pattern of the substrate annealed at 600 °C is also included. The peaks have been labelled according to the existing crystallographic phases (between parentheses, the used symbol to represent the phase together with its ICDD File Card no.): $BiFeO_3$ (§, 01-072-2321), $Bi_2Fe_4O_9$ (#, 01-072-1832), $Bi_{24}Fe_2O_{39}$ (+, 00-042-0201), Bi_2O_3 ([, 00-045-1344), α-Fe_2O_3 (=, 01-085-0987), γ-Fe_2O_3 (/, 00-039-1346), Fe_3O_4 (×, 00-001-1111), $Bi_4(SiO_4)_3$ (*, 01-088-0243) and CuO (^, 00-041-0254).

$Bi_4(SiO_4)_3$. At this temperature, the crystallite size of the $Bi_2Fe_4O_9$ significantly grows, reaching a value above 200 nm which cannot be estimated by line profile analysis.[44] At the same time, the amount of BFO strongly diminishes and the residual BFO is highly nanostructured as evidenced by its weak and broad XRD peaks, respectively (note that the BFO peaks located at 31.8 and 32.1 degrees nearly vanish upon annealing at 800 °C).

The film annealed at 700 °C was investigated by TEM (Fig. 3). The occurrence of both $Bi_2Fe_4O_9$ and $BiFeO_3$ phases was seen in the Fast Fourier Transform (FFT) patterns taken on different areas of the sample, in agreement with XRD results.

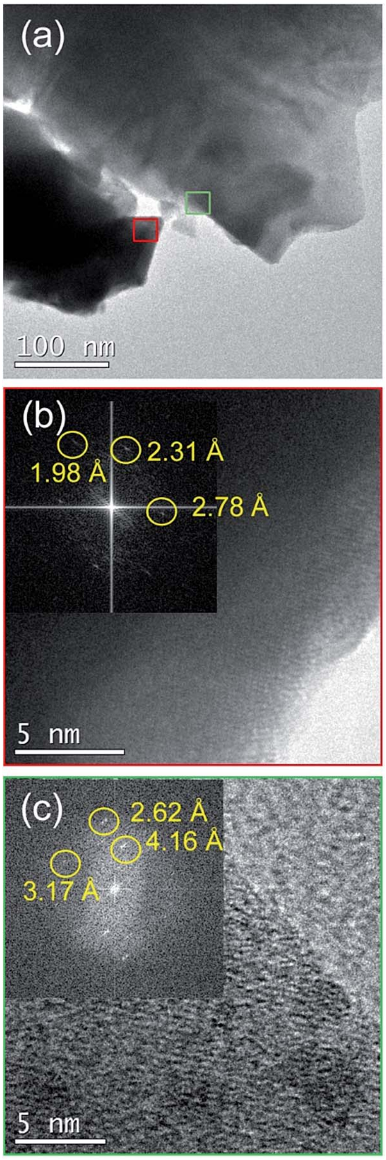

Fig. 3 (a) TEM image of a representative zone of the sample annealed at 700 °C. (b) HRTEM image of the red square depicted in panel (a). The inset corresponds to its FFT. The interplanar distances are characteristic of $Bi_2Fe_4O_9$. (c) HRTEM image of the green square illustrated in panel (a). The inset corresponds to its FFT and the interplanar distances belong to $BiFeO_3$ phase.

As aforementioned, the as-prepared sample is not fully dense. Moreover, the film is very rough (Fig. 1c). Even though the thermal treatment at 500 °C leads to a somewhat denser film, the 'open' structure remains (Fig. 4a). It is at 600 °C where the morphology starts to evolve towards more particulate-like, although some voids are still preserved. The particles adopt prism morphologies, indicating the formation of rhombohedral BFO (Fig. 4b). This is in concordance with the XRD analysis, which reveals that 500 °C is still a mild condition for the formation of BFO. With further increase of the annealing temperature (*i.e.*, 700 °C), the size of the particles slightly increases and the prism morphology becomes more well-defined (Fig. 4c). At 800 °C, even though the prism morphology remains, a significant particle coarsening occurs, resulting in a significant increase of the size of the particles. This is in agreement with the structural analysis which indicates that the crystallite size of the $Bi_2Fe_4O_9$ phase increases upon annealing at 800 °C up to values that cannot even be estimated by Rietveld refinement.

Magnetic characterisation

Magnetisation (M) *vs.* applied magnetic field (H_{applied}) curves (*i.e.*, hysteresis loops) are shown in Fig. 5. The as-prepared sample already exhibits traces of ferromagnetism which might be ascribed to Fe-rich areas in the amorphous oxide films.

Crystallisation takes place upon heat treatment. Annealing at 500 °C results in a slightly increased saturation magnetization, which might be ascribed to the residual formation of iron oxides (see Fig. 5 and Table 1). At room temperature, α-Fe_2O_3 shows weak ferromagnetic-like behaviour due to its nanoscale nature[45,46] and Fe_3O_4 and γ-Fe_2O_3 are ferromagnetic.[47] On top of this, BFO may also contribute to ferromagnetism due to size effects which result in antiferromagnetic spin canting due to the suppression of the spiral spin structure.[12–14,48] From a magnetic point of view, the ternary phases play a minor role since they are usually paramagnetic at room temperature.[49,50] For instance, $Bi_2Fe_4O_9$ becomes antiferromagnetic but only

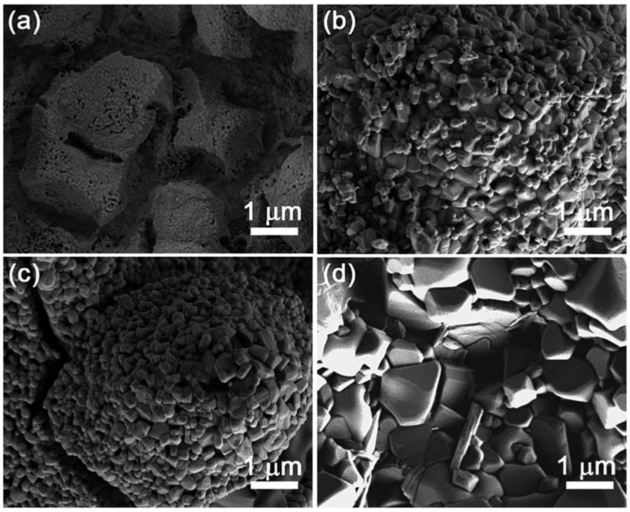

Fig. 4 SEM images, taken with secondary electrons, of the samples annealed at (a) 500, (b) 600, (c) 700 and (d) 800 °C.

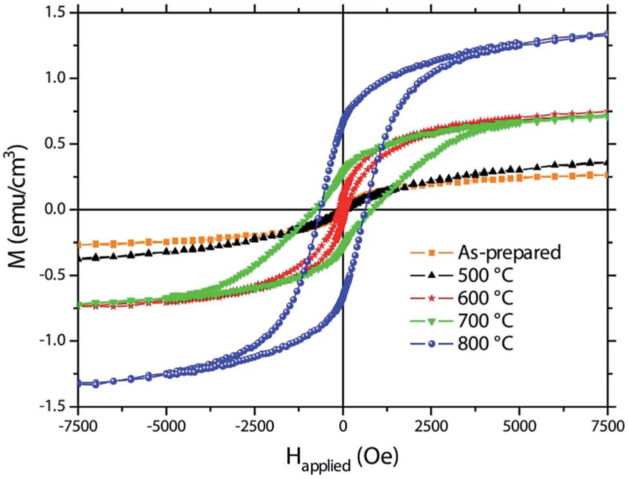

Fig. 5 Hysteresis loops recorded by vibrating sample magnetometry of the as-prepared sample and the samples annealed at 500, 600, 700 and 800 °C.

Table 1 Saturation magnetization, M_S, coercivity, H_C and remanence-to-saturation magnetization ratio, M_R/M_S, of the hysteresis loops presented in Fig. 5, which correspond to the as-prepared sample and the samples annealed at 500, 600, 700 and 800 °C

Sample	M_S (emu cm^{-3})	H_C (Oe)	M_R/M_S (%)
As-prepared	0.275	<40	<2.5
500 °C	0.390	<40	<2.5
600 °C	0.770	85	11.0
700 °C	0.745	822	38.3
800 °C	1.360	640	48.9

below 250 K.[50] At 600 °C, the saturation magnetisation significantly increases. From the structural and morphological analyses, this is accompanied with the formation of a nearly pure BFO in detriment of both Fe-based oxides and ternary phases (Fig. 2). Therefore, the observed ferromagnetic response could be primarily ascribed to nanostructuring effects which reinforce antiferromagnetic spin canting, giving rise to a larger net magnetisation. While the sample annealed at 700 °C shows a similar M_S than that of the sample annealed at 600 °C (Table 1), the saturation magnetisation of the sample annealed at 800 °C is considerably larger. The pronounced decomposition of BFO upon annealing at 800 °C yields a highly nanostructured phase with strong size effects which might be responsible for the increase in M_S. Taking into account the described structural changes with temperature, the increase in H_C upon annealing at 700 °C and 800 °C might also be related to the formation of $Bi_2Fe_4O_9$ and the other paramagnetic phases, which probably tends to isolate the BFO grains, thus decreasing intergranular dipolar and exchange interactions, both of which are known to be detrimental for coercivity.[51]

Conclusions

The synthesis of bismuth ferrite ($BiFeO_3$, BFO) has been successfully carried out by potentiostatic electrodeposition from a nitrate-based DMF bath followed by heat treatment in air. Since the electrodeposition results in amorphous-like films, thermal treatments are needed to induce crystallisation. Annealing procedures in air at 500, 600, 700 and 800 °C for 2 hours have been carried out. The heat treatment at 600 °C results in nearly pure nanostructured BFO with soft ferromagnetic-like properties. A detailed structural, morphological and magnetic characterisation as a function of annealing temperature evidences that BFO forms in a narrow temperature window. Moreover, the observed ferromagnetism is mainly ascribed to nanostructuration and is also sensitive to the presence of secondary phases, such as Bi–Fe–O ternary phases or iron oxides. Future investigations will focus on further optimization of the bath and annealing conditions in order to synthesize BFO with higher purity. It is envisaged that the electrodeposition of BFO in the form of films with increased surface area will emerge as a subject of interest that will inspire both new fundamental physics and device applications.

Acknowledgements

Financial support by the European Research Council (SPIN-PORICS 2014-Consolidator Grant, Agreement No. 648454), the Spanish Government (Project MAT2014-57960-C3-1-R and associated FEDER), and the Generalitat de Catalunya (2014-SGR-1015) and the European Union's Horizon 2020 research and innovation programme under the Marie Skłodowska-Curie grant agreements No. 642642 and 665919 is acknowledged. E. P. is grateful to MINECO for the "Ramón y Cajal" contract (RYC-2012-10839). J. F. acknowledges the "Juan de la Cierva" fellowship from MINECO (IJCI-2015-27030).

References

1 N. Izyumskaya, Y. Aliyov and H. Morkoç, *Crit. Rev. Solid State Mater. Sci.*, 2009, **34**, 89.
2 G. Catalan and J. F. Scott, *Adv. Mater.*, 2009, **21**, 2463.
3 B. Dieny, R. C. Sousa, J. Herault, C. Papusoi, G. Prenat, U. Ebels, D. Houssameddine, B. Rodmacq, S. Auffret, L. D. Buda-Prejbeanu, M. C. Cyrille, B. Delaet, O. Redon, C. Ducruet, J.-P. Nozieres and I. L. Prejbeanu, *Internet J. Nanotechnol.*, 2010, **7**, 591.
4 J.-M. Hu, Z. Li, L.-Q. Chen and C.-W. Nan, *Nat. Commun.*, 2011, **2**, 553.
5 T. Zhao, A. Scholl, F. Zavaliche, K. Lee, M. Barry, A. Doran, M. P. Cruz, Y. H. Chu, C. Ederer, N. A. Spaldin, R. R. Das, D. M. Kim, S. H. Baek, C. B. Eom and R. Ramesh, *Nat. Mater.*, 2006, **5**, 823.
6 R. Palai, R. S. Katiyar, H. Schmid, P. Tissot, S. J. Clark, J. Robertson, S. A. T. Redfern, G. Catalan and J. F. Scott, *Phys. Rev. B: Condens. Matter Mater. Phys.*, 2008, **77**, 014110.
7 M. Valant, A. K. Axelsson and N. Alford, *Chem. Mater.*, 2007, **19**, 5431.
8 S. M. Selbach, M. A. Einarsrud and T. Grande, *Chem. Mater.*, 2009, **21**, 169.
9 G. D. Achenbach, W. J. James and R. Gerson, *J. Am. Ceram. Soc.*, 1967, **50**, 437.

10 T. Liu, Y. Xu and J. Zhao, *J. Am. Ceram. Soc.*, 2010, **93**, 3637.

11 H. Yang, Y. Q. Wang, H. Wang and Q. X. Jia, *Appl. Phys. Lett.*, 2010, **96**, 012909.

12 M. Ramazanoglu, M. Laver, W. Ratcliff II, S. M. Watson, W. C. Chen, A. Jackson, K. Kothapalli, S. Lee, S.-W. Cheong and V. Kiryukhin, *Phys. Rev. Lett.*, 2011, **107**, 207206.

13 F. Z. Huang, Z. J. Wang, X. M. Lu, J. T. Zhang, K. L. Min, W. W. Lin, R. X. Ti, T. T. Xu, J. He, C. Yue and J. S. Zhu, *Sci. Rep.*, 2013, **3**, 2907.

14 H. Béa, M. Bibes, S. Petit, J. Kreisel and A. Barthélémy, *Philos. Mag. Lett.*, 2007, **87**, 165.

15 T. E. Quickel, L. T. Schelhas, R. A. Farrell, N. Petkov, V. H. Le and S. H. Tolbert, *Nat. Commun.*, 2015, **6**, 6562.

16 S. Y. Yang, L. W. Martin, S. J. Byrnes, T. E. Conry, S. R. Basu, D. Paran, L. Reichertz, J. Ihlefeld, C. Adamo, A. Melville, Y. H. Chu, C. H. Yang, J. L. Musfeldt, D. G. Schlom, J. W. Ager and R. Ramesh, *Appl. Phys. Lett.*, 2009, **95**, 062909.

17 S. Y. Yang, J. Seidel, S. J. Byrnes, P. Shafer, C. H. Yang, M. D. Rossell, P. Yu, Y. H. Chu, J. F. Scott, J. W. Ager, L. W. Martin and R. Ramesh, *Nat. Nanotechnol.*, 2010, **5**, 143.

18 M. Alexe and D. Hesse, *Nat. Commun.*, 2011, **2**, 256.

19 D. Huang, H. Deng, P. Yang and J. Chu, *Mater. Lett.*, 2010, **64**, 2233.

20 X. Wang, Y. G. Zhang and Z. B. Wu, *Mater. Lett.*, 2010, **64**, 486.

21 J. Wang, J. B. Neaton, H. Zheng, V. Nagarajan, S. B. Ogale, B. Liu, D. Viehland, V. Vaithyanathan, D. G. Schlom, U. V. Waghmare, N. A. Spaldin, K. M. Rabe, M. Wuttig and R. Ramesh, *Science*, 2003, **299**, 1719.

22 K. Jiang, J. J. Zhu, J. D. Wu, J. Sun, Z. G. Hu and J. H. Chu, *ACS Appl. Mater. Interfaces*, 2011, **3**, 4844.

23 P. S. Plyaka and G. N. Tolmachev, *Tech. Phys. Lett.*, 2010, **36**, 192.

24 K. Sarkar, S. Mukherjee and S. Mukherjee, *Process. Appl. Ceram.*, 2015, **9**, 53.

25 A. Hardy, S. Gielis, H. Van den Rul, J. D'Haen, M. K. Van Bael and J. Mullens, *J. Eur. Ceram. Soc.*, 2009, **29**, 3007.

26 N. Das, R. Majumdar, A. Sen and H. S. Maiti, *Mater. Lett.*, 2007, **61**, 2100.

27 E. A. V. Ferri, I. A. Santos, E. Radovanovic, R. Bonzaninic and E. M. Girotto, *J. Braz. Chem. Soc.*, 2008, **19**, 1153.

28 C. Ponzoni, M. Cannio, D. N. Boccaccini, C. R. H. Bahl, K. Agersted and C. Leonelli, *Mater. Chem. Phys.*, 2015, **162**, 69.

29 S. Mohan and B. Subramanian, *RSC Adv.*, 2013, **3**, 23737.

30 F. Gao, Y. Yuan, K. F. Wang, X. Y. Chen, F. Chen, J.-M. Liu and Z. F. Ren, *Appl. Phys. Lett.*, 2006, **89**, 102506.

31 T. J. Park, Y. B. Mao and S. S. Wong, *Chem. Commun.*, 2004, **23**, 2708.

32 C. Chen, J. R. Cheng, S. W. Yu, L. J. Che and Z. Y. Meng, *J. Cryst. Growth*, 2006, **291**, 135.

33 S. D. Sartale, C. D. Lokhande, M. Giersig and V. Ganesan, *J. Phys.: Condens. Matter*, 2004, **16**, 773.

34 A. Quintana, A. Varea, M. Guerrero, S. Suriñach, M. D. Baró, J. Sort and E. Pellicer, *Electrochim. Acta*, 2015, **173**, 705.

35 T. Yousefi, A. N. Golikand, M. H. Mashhadizadeh and M. Aghazadeh, *Curr. Appl. Phys.*, 2012, **12**, 193.

36 P. N. Bartlett, S. L. Benjamin, C. H. de Groot, A. L. Hector, R. M. Huang, A. Jolleys, G. P. Kissling, W. Levason, S. J. Pearce, G. Reid and Y. D. Wang, *Mater. Horiz.*, 2015, **2**, 420.

37 T. P. Gujar, V. R. Shinde, S. S. Kulkarni, H. M. Pathan and C. D. Lokhande, *Appl. Surf. Sci.*, 2006, **252**, 3585.

38 V. V. Jadhav, M. K. Zate, S. Liu, M. Naushad, R. S. Mane, K. N. Hui and S. H. Han, *Appl. Nanosci.*, 2016, **6**, 511.

39 T. P. Gujar, V. R. Shinde, C. D. Lokhande, R. S. Mane and S. H. Han, *Electrochem. Solid-State Lett.*, 2007, **10**, D1.

40 L. Lutterotti and P. Scardi, *J. Appl. Crystallogr.*, 1990, **23**, 246.

41 MAUD (Materials Analysis Using Diffraction), http://maud.radiographema.com/.

42 C. Q. Cui, S. P. Jiang and A. C. C. Tseung, *J. Electrochem. Soc.*, 1991, **138**, 94.

43 M. K. Tripathi, D. K. Singh and V. B. Singh, *J. Electrochem. Soc.*, 2015, **162**, D87.

44 B. D. Cullity, *Elements of X-ray Diffraction*, Addison-Wesley Publishing Company, Inc., USA, 1956.

45 Z. Y. Sun, H. Q. Yuan, Z. M. Liu, B. X. Han and X. R. Zhang, *Adv. Mater.*, 2005, **17**, 2993.

46 S. Sakurai, A. Namai, K. Hashimoto and S. Ohkoshi, *J. Am. Chem. Soc.*, 2009, **131**, 18299.

47 R. Masrour, E. K. Hlil, M. Hamedoun, A. Benyoussef, O. Mounkachi and H. El Moussaou, *J. Magn. Magn. Mater.*, 2015, **378**, 37.

48 H. Modarresi, V. Lazenka, E. Menéndez, M. Lorenz, M. Bisht, A. Volodin, C. Van Haesendonck, M. Grundmann, M. J. Van Bael, K. Temst and A. Vantomme, *J. Phys. D: Appl. Phys.*, 2016, **49**, 325302.

49 A. A. Zatsiupaa, L. A. Bashkirov, I. O. Troyanchuk, G. S. Petrov, A. I. Galyas, L. S. Lobanovsky and S. V. Truhanov, *J. Solid State Chem.*, 2014, **212**, 147.

50 Z. Irshad, Z. H. Shah, M. A. Rafiq and M. M. Hasan, *J. Alloys Compd.*, 2015, **624**, 131.

51 R. Skomski and J. M. D. Coey, *Permanent Magnetism*, Institute of Physics Publishing, Bristol and Philadelphia, 1999.